

1 Ozone Variability Induced by Synoptic Weather Patterns
2 in Warm Seasons of 2014–2018 over the Yangtze River
3 Delta Region, China

4 Da Gao¹, Min Xie^{1*}, Jane Liu^{2,3}, Tijian Wang¹, Chaoqun Ma^{1,a}, Haokun Bai¹, Xing Chen¹,
5 Mengmeng Li¹, Bingliang Zhuang¹, Shu Li¹

6 ¹ School of Atmospheric Sciences, Joint Center for Atmospheric Radar Research of CMA/NJU,
7 CMA-NJU Joint Laboratory for Climate Prediction Studies, Jiangsu Collaborative Innovation
8 Center for Climate Change, Nanjing University, Nanjing 210023, China

9 ² College of Geographic Sciences, Fujian Normal University, Fuzhou 350007, China

10 ³ Department of Geography and Planning, University of Toronto M5S 3G3, Canada

11 ^a now at: Minerva Research Group, Max Planck Institute for Chemistry, Mainz, Germany

12 -----

13 * Corresponding author. School of Atmospheric Sciences, Nanjing University, Nanjing 210023,
14 China. minxie@nju.edu.cn (M. Xie)

15
16 **Abstract:** Ozone (O₃) pollution is of great concern in the Yangtze River Delta (YRD) region of
17 China, and the regional O₃ pollution is closely associated with dominant weather systems. With a
18 focus on the warm seasons (April–September) from 2014 to 2018, we quantitatively analyze the
19 characteristics of O₃ variations over the YRD, the impacts of large-scale and synoptic-scale
20 circulations on the O₃ variations and the associated meteorological controlling factors, based on
21 observed ground-level O₃ and meteorological data. Our analysis suggests an increasing trend of the
22 regional mean O₃ concentration in the YRD at 1.81 ppb per year over 2014–2018. Spatially, the
23 empirical orthogonal function analysis suggests the dominant mode accounting for 65.70% variation
24 in O₃, implying that an increase in O₃ is the dominant tendency in the entire YRD. Meteorology is
25 estimated to increase the regional mean O₃ concentration by 3.03 ppb at most from 2014 to 2018.
26 Especially, relative humidity (RH) plays the most important role in modulating the inter-annual O₃
27 variation, followed by solar radiation (SR) and low cloud cover (LCC). As atmospheric circulations
28 can affect local meteorological factors and O₃ levels, we identify five dominant synoptic weather
29 patterns (SWPs) in the warm seasons in the YRD using the t-mode principal component analysis

30 classification. The typical weather systems of SWPs include the western Pacific Subtropical High
31 (WPSH) under SWP1, a continental high and the Aleutian low under SWP2, an extratropical
32 cyclone under SWP3, a southern low pressure and WPSH under SWP4 and the north China
33 anticyclone under SWP5. The variations of the five SWPs are all favorable to the increase in O₃
34 concentrations over 2014–2018. However, crucial meteorological factors leading to increases in O₃
35 concentrations are different under different SWPs. These factors are identified as significant
36 decreases in RH and increases in SR under SWPs 1, 4 and 5, significant decreases in RH, increases
37 in SR and air temperature (T2) under SWP2, and significant decreases in RH under SWP3. Under
38 SWPs 1, 4 and 5, significant decreases in RH and increases in SR are predominantly caused by the
39 WPSH weakening under SWP1, the southern low pressure weakening under SWP4, and the north
40 China anticyclone weakening under SWP5. Under SWP2, significant decreases in RH, increases in
41 SR and T2 are mainly produced by the Aleutian low southward extending and a continental high
42 weakening. Under SWP3, significant decreases in RH is mainly induced by an extratropical cyclone
43 strengthening. These changes in atmospheric circulations prevent the water vapor in the southern
44 and northern sea from being transported to the YRD and result in RH significantly decreasing under
45 each SWP. In addition, strengthened descending motions (behind the strengthening trough and in
46 front of the strengthening ridge) lead to decreases in LCC and significant increases in SR under
47 SWP1, 2, 4 and 5. The significant increases in T2 would be due to weakening cold flow introduced
48 by a weakening continental high. Most importantly, the changes in the SWP intensity can make
49 large variations in meteorological factors and contribute more to the O₃ inter-annual variation than
50 the changes in the SWP frequency. Finally, we reconstruct an EOF mode 1 time series that is highly
51 correlated with the original O₃ time series, and the reconstructed time series performs well in
52 defining the change in SWP intensity according to the unique feature under each of the SWPs.

53

54 **1. Introduction**

55 As an air pollutant, surface ozone (O₃) is harmful to human health and vegetation growth, such
56 as damaging human lungs (Jerrett et al. 2009; Day et al. 2017) and destroying forest and agricultural
57 crops (Yue et al. 2017). After the emission control following “Thirteenth Five-Year Plan”
58 Comprehensive Work Plan for Energy Saving and Emission Reduction in China since 2016,
59 concentrations of many pollutants have decreased over the past few years in China, but not for O₃.

60 Furthermore, heavy O₃ pollution episodes occur more frequently and more severely in China than
61 in Japan, South Korea, the United States, and the European countries (Lu et al. 2018). Li et al. (2018)
62 proposed that the rapid decrease of fine particulate matter (PM) in China is a reason for such O₃
63 increase as aerosol sinks of hydro-peroxy radicals are reduced. Yet, meteorological influences on
64 the O₃ increase are unclear and require further investigations.

65 Surface O₃ is mainly formed through complex and nonlinear photochemical reactions of volatile
66 organic compounds (VOCs) and nitrogen oxides (NO_x) exposed to the sunlight (Xie et al. 2014).
67 Meteorology can affect O₃ levels through modulation of photochemical reactions, advection,
68 convection and turbulent transport, as well as dry and wet depositions (Liu et al. 2013; Xie et al.,
69 2016a, 2016b). Synoptic weather patterns (SWPs) and the associated meteorological conditions can
70 impact long-term and daily O₃ variations (Hegarty et al. 2007; Santurtún et al. 2015; Gao et al. 2020;
71 Shu et al., 2020). Understanding the mechanisms of meteorological influences on O₃ variations and
72 quantifying such influences would help to understand the formation of O₃ pollution.

73 Previous studies have revealed that severe O₃ pollution episodes are usually accompanied with
74 high temperature, strong solar radiation, drying condition and stagnant weather (Jacob and Winner
75 2009; Doherty et al. 2013; Shu et al. 2016; Pu et al. 2017; Zhang et al. 2018), and these local
76 meteorological conditions are often related to specific synoptic-scale and large-scale atmospheric
77 circulation systems (Fiore et al. 2003; Leibensperger et al. 2008; Barnes and Fiore. 2013; Shu et al.
78 2016; Wang et al. 2016; Zhao and Wang. 2017). For example, O₃ pollution in the eastern United
79 States is notably influenced by the cyclone frequency (Leibensperger et al. 2008), latitude of the
80 polar jet over eastern North America (Barnes and Fiore. 2013) and the behavior of the quasi-
81 permanent Bermuda High (Fiore et al. 2003; Wang et al. 2016). In China, Yang et al. (2014)
82 illustrated that the changes in meteorological variables, associated with the East Asian summer
83 monsoon, lead to 2–5 % inter-annual variations in surface O₃ concentrations over the central-eastern
84 China. Zhao and Wang (2017) found that a significantly strong western Pacific subtropical high
85 (WPSH) could result in higher relative humidity (RH), more clouds, more rainfall, and less
86 ultraviolet radiation, finally leading to less O₃ formation. Using model simulation, Shu et al. (2016)
87 investigated the synergistical impact of the WPSH and typhoons on O₃ pollution in Yangtze River
88 Delta region.

89 As known, a region is influenced by different weather systems. Weather classification, as a way
90 to distinguish the different large-scale and synoptic-scale atmospheric circulation systems, is widely
91 used in exploring connections between weather patterns and O₃ levels (Han et al. 2020; Gao et al.
92 2020). Gao et al. (2020) discussed i
93 nfluences of six SWPs on O₃ levels in the YRD, and revealed differences in O₃ pollution levels
94 due to minor changes in atmospheric circulations. However, it is uncertain that how changes in the
95 SWPs could lead to O₃ pollution in detail, especially in the YRD. For the northern China and the
96 PRD region, Liu et al. (2019) quantified the impact of synoptic circulation patterns on O₃ variability
97 in the northern China from April to October during 2013–2017. Yang et al. (2019) quantitatively
98 assessed the impacts of meteorological factors and the precursor emissions on the long-term trend
99 of ambient O₃ over the PRD region. However, whether variations in SWPs can lead to O₃ increases
100 in recent years over the YRD has not be sufficiently addressed.

101 Due to the recent increases in O₃ level over the YRD (Gao et al. 2017; Xie et al. 2017), studies
102 on characterizing the O₃ variation in the region and understanding the mechanisms for the variation
103 are urgently required. To this end, the temporal and spatial variations in surface O₃ including 5-year
104 trend over the YRD are quantitatively investigated, and the mechanisms of meteorological
105 influences on the O₃ variations are analyzed. Especially, the characteristics of the corresponding
106 SWPs are discussed in detailed. The remainder of this paper is organized as follows. Data and
107 methods are introduced in section 2. The inter-annual variation and 5-year trend and spatial variation
108 characteristics of surface ozone in the YRD are illustrated in section 3.1. The impact of
109 meteorological factors on the O₃ variation is discussed in section 3.2. The main SWPs and the effects
110 of their changes on the O₃ variation are described in section 3.3. Section 3.4 discusses the
111 contributions of the changes in SWP intensity and frequency to the inter-annual variation and trend
112 of O₃. Finally, the conclusion and discussions are shown in section 4.

113

114 **2. Data and methods**

115 **2.1. O₃ and meteorological datasets**

116 The maximum daily 8-hours average O₃ data are available from the National Environmental
117 Monitoring Center of China, which were acquired from the air quality real-time publishing platform
118 (<http://106.37.208.233:20035>). The hourly observation data of meteorological factors including air

119 temperature (T2), RH and wind speed (WS) in the warm seasons from April to September over
120 2014–2018 were acquired from the National Meteorological Center of China Meteorological
121 Administration (<http://eng.nmc.cn>). 26 cities are selected as typical cities representative of the YRD
122 according to the “Urban agglomeration on Yangtze River Delta” approved by China’s State Council
123 in 2016. There are total 172 stations in 26 cities. In order to better characterize the O₃ pollution
124 levels of each city, the hourly O₃ concentration of each city is calculated as the average value of the
125 O₃ concentrations measured in several of the national monitoring sites in that city. In this paper, the
126 term "O₃ concentration" refers to the maximum daily 8-hours average O₃ concentration unless stated
127 otherwise.

128

129 **2.2. Linear trend analyses**

130 To characterize the O₃ variation in the warm seasons during 2014–2018 over the YRD, a
131 linear trend method based on monthly anomalies is used (see Equation 1), which has been widely
132 used to calculate the trends of time series with seasonal cycles and autocorrelation. The O₃ monthly
133 anomalies are more precise than O₃ monthly means because the impact of missing data is reduced.
134 In addition, hourly O₃ data and fewer yearly O₃ data are inappropriate to use because of too many
135 temporal variation signals and easily overfitting. Using this method, Cooper et al. (2020) and Lu et
136 al. (2020) quantified the O₃ trend in 27 globally distributed remote locations and the whole China.
137 Anomalies of monthly average O₃ concentration are defined as the difference between the individual
138 monthly mean and the monthly mean of 2014–2018. The parametric linear trend is calculated by
139 using the generalized least-squares method with auto-regression.

$$140 \quad y_t = b + kt + \alpha \cos\left(\frac{2\pi M}{6}\right) + \beta \sin\left(\frac{2\pi M}{6}\right) + R_t \quad (1),$$

141 where y_t represents the monthly anomaly, t is the monthly index from April to September during
142 2014–2018, b denotes the intercept, k is the linear trend, α and β are coefficients for a 6-
143 month harmonic series (M ranges from 1 to 6) which is used to account for potentially remaining
144 seasonal signals, and R_t represents a normal random error series. In this study, linear trend k is
145 regarded as the inter-annual O₃ variation trend and is discussed in section 3.1.1.

146

147 **2.3. Meteorological adjustment**

148 The meteorological adjustment, a statistical method, is applied to quantify the impact of
 149 meteorology on O₃ variation through removing such impact in the original O₃ data. It is similar to a
 150 model simulation that keeps the emission levels fixed but allows meteorology to vary. Yet, this
 151 method requires much less computing resources than a model simulation. The method is introduced
 152 in detail as follows.

153 In the meteorological adjustment, the observed O₃ and meteorological data are separated into
 154 long-term, seasonal, and short-term data (Rao and Zurbenko 1994a, b). The Kolmogorov-Zurbenko
 155 (KZ) filter can be expressed as follows.

$$156 \quad R(t) = L(t) + S(t) + W(t) \quad (2),$$

157 where $R(t)$ represents the raw time series data, $L(t)$ the long-term trend on a timescale of years,
 158 $S(t)$ the seasonal variation on a timescale of months, and $W(t)$ the short-term component on a
 159 timescale of days.

160 In order to remove the high-pass signal, the KZ filter carries out p times of iterations of a
 161 moving average with the window length m , which is defined as

$$162 \quad Y_i = \frac{1}{m} \sum_{j=-k}^k R_{i+j} \quad (3)$$

163 where R is the original time series, i an index for the time of iteration, j an index for sampling inside
 164 the window, and k the number of sampling on one side of the window. The window length $m = 2k$
 165 $+1$. Y is the input time series after one iteration. Different scales of motions are obtained by changing
 166 the window length and the number of iterations (Milanchus et al. 1998; Eskridge et al. 1997). The
 167 filter periods of less than N days can be calculated with window length m and the number of
 168 iteration p , as follows:

$$169 \quad m \times p^{\frac{1}{2}} \leq N \quad (4).$$

170 Therefore, the cycles of 33 days can be removed by a KZ(15, 5) filter with the window length of 15
 171 and 5 iterations. In Equation 5, BL(t) is the O₃ and meteorological time series obtained by KZ(15,5)
 172 filter and refers to their baseline variations which are the sum of the long term $L(t)$ and the seasonal
 173 component $S(t)$.

$$174 \quad BL(t) = KZ_{(15,5)} = L(t) + S(t) = KZ_{(183,3)} + S(t) \quad (5).$$

175 The long-term trend is separated from the raw data obtained by KZ (183, 3) with the periods of $>$
 176 632 days, and then the seasonal and the short-term component $W(t)$ can be defined as

177 $S(t) = KZ_{(15,5)} - KZ_{(183,3)} \quad (6),$

178 $W(t) = X(t) - BL(t) = X(t) - KZ_{(15,5)} \quad (7).$

179 After KZ filtering, the meteorological adjustment is conducted by the multivariate regression
 180 between the O₃ concentration and meteorological factors such as T, RH, wind speed and sunshine
 181 duration (Wise and Comrie 2005; Papanastasiou et al. 2012).

182 $A_{BL}(t) = a_{BL} + \sum b_{BLi} \cdot M_{BLi} + \epsilon_{BL}(t) \quad (8),$

183 $A_W(t) = a_W + \sum b_{Wi} \cdot M_{Wi} + \epsilon_W(t) \quad (9),$

184 $\epsilon(t) = \epsilon_{BL}(t) + \epsilon_W(t) \quad (10),$

185 $A_{ad}(t) = \epsilon(t) + \sum b_{BLi} \cdot \overline{M}_{BLi} + \sum b_{Wi} \cdot \overline{M}_{Wi} + a_{BL} + a_W \quad (11).$

186 the multivariate regression models between baseline and short-term O₃ and meteorological factors
 187 are shown in Equations 8 and 9. The $A_{BL}(t)$ and M_{BLi} represent the sum of the long term L(t) and
 188 the seasonal component S(t) of O₃ concentration and meteorological factors. The $A_W(t)$ and
 189 M_{Wi} represent the short-term W(t) of O₃ concentration and meteorological factors. The a and b
 190 are the fitted parameters, and i is time point (days). $\epsilon(t)$ is the residual term. The average
 191 meteorological condition \overline{M} at the same calendar date during the 5 years is regarded as the base
 192 condition for that date, and the meteorological adjustment is conducted against the base condition.
 193 In these steps, $A_{ad}(t)$ refers to the meteorologically adjusted O₃ variation with the homogenized
 194 annual variation in meteorological conditions. The difference between raw O₃ time series and
 195 $A_{ad}(t)$ represents the meteorological impact.

196

197 **2.4. Classification of SWPs**

198 In order to find the detailed variation characteristics of SWPs, we first extract the predominant
 199 SWPs in the warm seasons over the YRD using a weather classification method. Common objective
 200 classification methods include using predefined type, the leader algorithm, the cluster analysis,
 201 optimization algorithms and eigenvectors (Philipp et al. 2016). The PTT method, a simplified
 202 variant of t-mode principal component analysis using orthogonal rotation, is used to classify SWPs
 203 during 2014–2018. It is one of the methods for weather classification in European Cooperation in
 204 Science and Technology Action 733 (Philipp et al. 2016), which is widely used in atmospheric
 205 sciences (Hou et al. 2019).

206

207 **2.5. FNL and ERA-Interim meteorological data**

208 The National Center for Environmental Prediction Final Operational Global Analysis (FNL)
209 data (<http://rda.ucar.edu/datasets/ds083.2/>) produced by the Global Data Assimilation System are
210 used in classifying SWPs and analyzing atmospheric circulations. The data have a horizontal
211 resolution of $2.5^{\circ} \times 2.5^{\circ}$, with 144×73 horizontal grids available every 6 hours. From the near surface
212 layer to 10 hPa, there are 17 pressure levels in the vertical direction. The data of the geopotential
213 height and wind at 500 hPa and 850 hPa, the vertical wind (Ω), temperature are used in this study.
214 At the same time, the low cloud cover (LCC), the total cloud liquid water (TCLW) and solar
215 radiation (SR) from ERA-interim are supplemented in this study, which have the same temporal and
216 spatial resolutions as the FNL data. Moreover, the western Pacific Subtropical High index (WPSHI)
217 and the eastern Asian summer monsoon index (EASMI) are calculated using the FNL data of the
218 geopotential height and wind at 850 hPa. The WPSHI is defined following the western Pacific
219 Subtropical High intensity index in the National Climate Center of China. Specific formula refers
220 to website (https://cmdp.ncc-cma.net/extreme/floods.php?product=floods_diag). The EASMI is a
221 shear vorticity index. It is defined as the difference of regional mean zonal wind at 850 hPa between
222 5 and 15°N , 22.5 and 32.5°N , 90 and 130°E , and 110 and 140°E in Wang and Fan (1999),
223 recommended by Wang et al. (2008).

224 The FNL geopotential height field at 850 hPa can capture the synoptic circulation variations
225 over the YRD well (Shu et al. 2017). In this study, we use the geopotential height at 850 hPa from
226 April to September during 2014–2018 as the input for the PTT. WPSHI and EASMI are correlated
227 with the O_3 time series. We used the Pearson correlation coefficient to calculate the correlations
228 between two time series.

229

230 **2.6. Reconstruction of O_3 concentration based on SWP**

231 To quantify the inter-annual variability captured by the variations (frequency and intensity) in
232 the SWPs, Yaranl (1992) provided an algorithm to find the contribution of SWPs frequency variation
233 to the inter-annual O_3 variation. The specific calculation is as follows.

$$234 \overline{\text{O}_{3m}}(fre) = \sum_{k=1}^6 \overline{\text{O}_{3k}} F_{km} \quad (12),$$

235 where $\overline{O_{3m}}(fre)$ is the reconstructed mean O_3 concentration influenced by the frequency variation
 236 in SWPs from April to September for year m , $\overline{O_{3k}}$ is the 5-year mean O_3 concentration for SWP
 237 k , and F_{km} is the occurrence frequency of SWP k during April–September for year m .

238 Hegarty et al. (2007) suggested that changes in the SWP include both frequency change and
 239 intensity change. The intensity of SWPs represents the location and strength of the weather system.
 240 Moreover, they noted that the environmental and climate-related contributions to the inter-annual
 241 variations of O_3 could be better separated by considering these two changes. So, Equation 12 is
 242 modified into the following form.

$$243 \quad \overline{O_{3m}}(fre + int) = \sum_{k=1}^6 (\overline{O_{3k}} + \Delta O_{3km}) F_{km} \quad (13),$$

244 where $\overline{O_{3m}}(fre + int)$ is the reconstructed average O_3 concentration influenced by the frequency
 245 and intensity changes of SWPs from April to September for year m ; ΔO_{3km} is the modified
 246 difference on the fitting line, which is obtained through a linear fitting of the annual O_3 concentration
 247 anomalies (ΔO_3) to the SWP intensity index (SWPII) for SWP k in year m . ΔO_{3km} represents the
 248 part of the annual observed O_3 oscillation caused by the intensity variation in each SWP. Hegarty et
 249 al. (2007) used the domain averaged sea level pressure to represent the circulation intensity index
 250 (CII). Liu et al. (2019) reconstructed the inter-annual O_3 level in the northern China using the center
 251 pressure of the lowest pressure system. However, we find the intensity variation in each SWP is
 252 different when O_3 increases. So we select different SWPII under each SWP according to the
 253 characteristics of high O_3 concentration. Lastly, we select the maximum height in zone-1 (25°N–
 254 40°N, 110°E–130°E), the maximum height in zone-2 (20°N–50°N, 90°E–140°E) and the mean
 255 height in zone-3 (10°N–40°N, 110°E–130°E). Especially, zones 1, 2 and 3 were selected in term of
 256 location of dominated weather systems under each SWP. Detailed demonstration is introduced in
 257 section 3.5.

258

259 **3. Results and discussion**

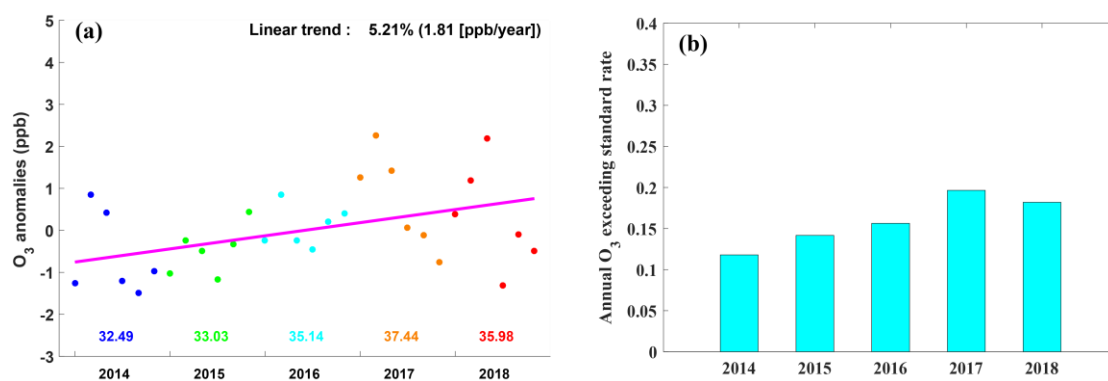
260 **3.1. Spatio-temporal variations of O_3 in the YRD region**

261 **3.1.1. Inter-annual variations of O_3**

262 Fig. 1a shows the time series of the anomalies of the monthly mean O_3 concentration over the
 263 YRD from April to September during 2014–2018, as well as the corresponding linear fitting curve.

264 Fig. 1b shows the annual variation in the total number of days with O₃ concentration exceeding the
 265 national standard during the warm seasons over 2014-2018. As shown in Fig. 1a, the monthly mean
 266 O₃ concentration in the warm seasons increases over 2014-2018, reaching the maximum of 37.44
 267 ppb in 2017 and maintaining at a high level in 2018. According to the generalized least-squares
 268 method with auto-regression in section 2.2, obtained fitting function is $y_t = -0.8076 +$
 269 $0.0521t - 0.4824 \cos\left(\frac{2\pi M}{6}\right) + 0.6646 \sin\left(\frac{2\pi M}{6}\right) + R_t$. Specifically, 5.21% (1.81 ppb) of k value
 270 as the O₃ inter-annual variation shows a large increasing trend in the YRD, which is slightly higher
 271 than that in the entire China (5.00% per year, Lu et al. 2020). Meanwhile, the annual average days
 272 with O₃ exceeding the standard during the warm seasons also show an increasing trend, reaching a
 273 peak in 2017 and maintaining at a high level in 2018. In all, both means and extremes of O₃
 274 concentration have increased over the YRD.

275



276

277 **Fig. 1. (a) Anomalies of monthly average O₃ concentration from April to September during**
 278 **2014–2018. The purple solid line represents the linear fitted curve ($y_t = -0.8076 + 0.0521t$),**
 279 **and the color number represents the annual (April–September) mean of O₃ concentration. (b)**
 280 **Annual (April–September) variation in the days with O₃ exceeding the national standard.**

281

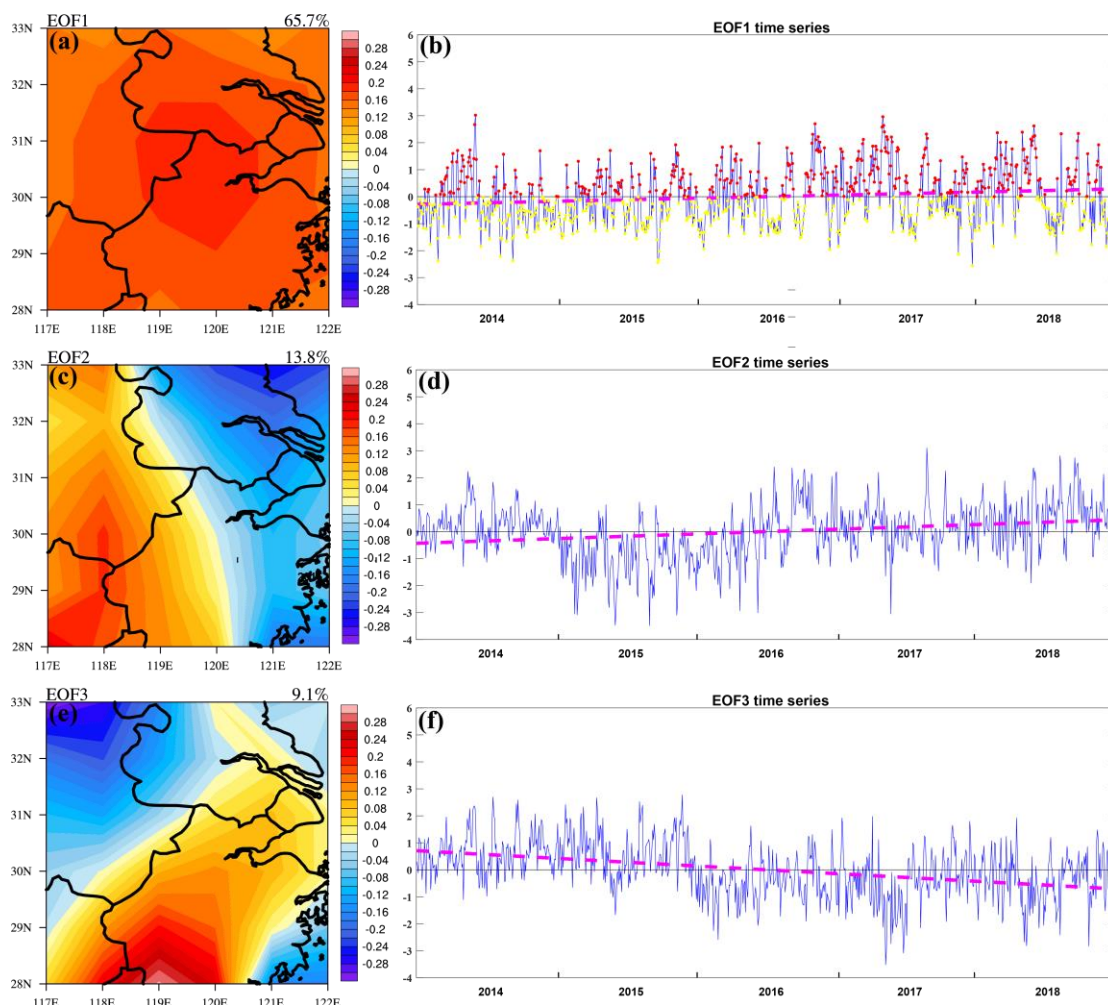
282 3.1.2. Characteristics of O₃ variability based on the EOF analysis

283 To further discuss the spatio-temporal distribution characteristics of the observed O₃
 284 concentration, the EOF approach is used to uncover the relationship between the spatial distribution
 285 and temporal variation. By removing the missing data for 17 days, O₃ concentrations in 898 days
 286 are processed. The percentages of variance contribution for the first three patterns are 65.70 %,
 287 13.80 % and 9.10 %, respectively. The significance tests of the EOF eigenvalue confirm that the

288 first three patterns are significantly separated. Approximately 88.60 % of the variability in the
289 original data is contained in these three patterns. In the first EOF pattern (EOF1), the observed O₃
290 over the YRD changes similarly and the center of the variation is located in the middle of the YRD
291 (Fig. 2a). As shown in Fig. 2b, the time series of EOF1 presents an increasing trend and shows a
292 high negative correlation with the time series of O₃ ($R = 0.98$). Therefore, to some extent, the EOF1
293 time series variation can represent the daily mean O₃ variation and implies an increasing trend of
294 regional mean O₃ concentration during these periods. Furthermore, we investigated the relationships
295 between the time series of EOF1 and different weather systems, as well as the meteorological factors.
296 Weather systems include the WPSH and the East Asian summer monsoon, which are dominant
297 weather systems affecting the YRD. Both of them show a poor correlation with the EOF1 time series
298 ($R_{WPSHI} = -0.13$ and $R_{EASMI} = -0.04$). It indicates that the daily O₃ variation is too complex to be
299 comprehensively explained through the change in a single weather system. Furthermore, the RH
300 and SR present a good correlation with the EOF1 time series ($R_{RH} = -0.59$ and $R_{SR} = 0.56$). However,
301 it is still unclear how the change in different weather systems causes the variation in RH and SR,
302 and how the variations in RH and SR impact the other meteorological factors and O₃ accumulation.

303 In the second EOF pattern (EOF2), there is obvious east-west contrast. In contrast, the third
304 EOF (EOF3) pattern presents a notable south-north contrast. At the same time, the increasing trend
305 of EOF2 time series and the decreasing trend of EOF3 time series indicate that O₃ concentrations in
306 the west and northwest have risen from 2014 to 2018. It implies that a higher rate of O₃ increasing
307 would occur in the northwest. As known, the variance contribution of EOF1 is 65.70 % that is
308 greater than EOF2 (13.80 %) and EOF3 (9.10 %). Therefore, increases in O₃ in the entire YRD
309 region is the main trend.

310



311

312 **Fig. 2. Three EOF patterns of O₃ concentration in the warm seasons from 2014 to 2018,**
 313 **including the spatial pattern (a, c and e) and time coefficient (b, d and f). The percentage in**
 314 **panels (a, c and e) is the variance contribution of each EOF mode. The pink dash line in panels**
 315 **(b, d and f) represents the linear fitted curve.**

316

317 **3.2. Effects of meteorological conditions on O₃ concentration over the YRD region**

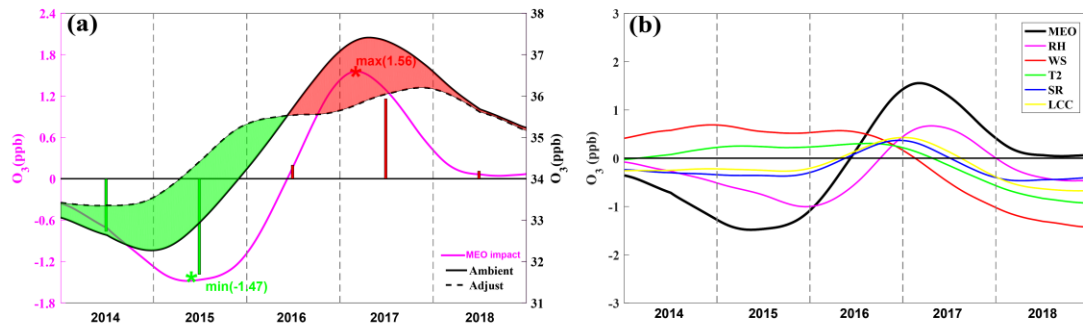
318 **3.2.1. Quantifying the effects of meteorological conditions**

319 With the primary pollutant emissions being cut down, the surface O₃ increase in the recent years
 320 in China might be attributable to a variety of factors, one of which was suggested to be the slowing
 321 down sink of hydroperoxy radicals, related to the variation in PM_{2.5} (Li et al. 2019). Yet, it is
 322 uncertain how meteorological conditions influence the increasing trend in surface O₃. Yang et al.
 323 (2019) quantified the meteorological impact on O₃ variation over the Pearl River Delta region using
 324 the meteorological adjustment. Using the methodology similar to that in Yang et al. (2019), we

325 investigate meteorological influences on the increase in ozone over the YRD in the warm seasons
326 during 2014–2018. Fig. 3a shows the ambient O₃ variation from 2014 to 2018: i.e. O₃ concentration
327 increases from 2014, reaches the maximum in 2017, and maintains at a relatively high level in 2018.
328 After the meteorological adjustment, the variable magnitude is lower than the original one, implying
329 that if the meteorological conditions remained unchanged over the 5 years, the variation in ambient
330 O₃ concentration would be lower. The meteorological impact can be examined from the difference
331 between the black solid and dashed lines in Fig. 3a. The difference is negative from 2014 to the
332 middle of 2016 and positive from middle of 2016 to 2018. In 2017, the meteorological conditions
333 increase O₃ concentration by about 1.16 ppb. However, in 2015, the meteorological conditions
334 become unfavorable to the O₃ accumulation, leading to an O₃ reduction of 1.39 ppb. The
335 meteorological conditions make a difference in O₃ concentration by 3.03 ppb at most between the
336 most favorable year (2017) and the most unfavorable year (2015), which roughly corresponds to
337 $8.70\% \left(\frac{\max(\text{MEO impact}) - \min(\text{MEO impact})}{\text{O}_3(5 \text{ year average})} \right)$ of the annual O₃ concentration.

338 In addition, we select the most influential meteorological factors to discuss their impacts on O₃
339 variation, including T2, RH, SR, LCC and WS. As shown in Fig. 3b, RH is the most crucial factor
340 and its variation is similar to the variation in the total meteorological impact. In addition, SR and
341 LCC also play important roles and have large impacts on O₃ variation. RH can impact O₃
342 concentration in two ways. One is gas phase H₂O reacting with O₃ ($\text{O}_3 + \text{H}_2\text{O}(\text{gas}) + h\nu \rightarrow \text{O}_2 +$
343 2OH). The other is its influencing on clouds and thereby shielding SR. The East Asian summer
344 monsoon plays a key role in affecting the local RH, and meanwhile it might bring a certain amount
345 of O₃ from the areas south of the YRD. However, O₃ concentration is high negatively related to RH,
346 which implies that the local chemical reaction might contribute to the O₃ accumulation more than
347 the regional transport. The impacts of T2 and WS are inconsistent with the overall meteorological
348 impacts.

349



350

351 **Fig. 3. (a) 5-year trends of ambient O₃ (solid black line), meteorological adjusted O₃ (dashed**
 352 **black line), and the meteorological impact (pink line) over the YRD during 2014–2018. Periods**
 353 **with positive and negative meteorological impacts are shaded in red and green, respectively;**
 354 **red and green bars represent the O₃ increases and decreases attributable to meteorological**
 355 **influences in each year. (b) 5-year variations in the meteorological impact of different**
 356 **meteorological factors (MEO), including relative humidity (RH), solar radiation (SR), air**
 357 **temperature (T2), wind speed (WS) and low cloud cover (LCC).**

358

359 3.3. Dynamic processes of O₃ variation driven by synoptic circulations

360 As discussed in section 3.2, the local meteorological factors have a large impact on the O₃
 361 variation. However, to some extent, the variation in local meteorological factors is largely affected
 362 by the synoptic-scale weather circulations (Leibensperger et al. 2008; Fiore et al. 2003; Wang et al.
 363 2016). For example, in summer the YRD is under a hot-wet environment controlled by the WPSH.
 364 While in winter it is under a cold-dry environment affected by the northwesterly flow caused by the
 365 Siberian High. The different weather systems under their corresponding SWPs have their unique
 366 meteorological characteristics. Moreover, even under one SWP, the location and intensity changes
 367 in a specific weather system can cause the changes in local meteorological factors correspondingly
 368 (Gao et al. 2020).

369

370 3.3.1. The main synoptic weather patterns in the warm season over the YRD

371 Applying the PTT classification method, nine SWPs are identified for the warm seasons in the
 372 YRD. Due to the relatively large variance, the first dominant five SWPs are selected, and the other
 373 four SWPs are grouped as ‘others’. As shown in Table 1, SWP1, SWP2 and SWP4 are dominant,

374 accounting for 40.66%, 22.84% and 13.99% of the occurrence frequency, respectively. In contrast,
 375 SWP3, SWP5 and other types occur in low frequencies, being 7.65%, 6.99% and 6.01%,
 376 respectively. Specifically, SWP1 is under control of the southwesterly flow introduced by the WPSH.
 377 SWP2 is influenced by the northwesterly flow introduced by a continental high pressure and the
 378 Aleutian low pressure. SWP4 is influenced by the southeasterly flow introduced by the WPSH and
 379 a cyclone. SWP3 and SWP5 are affected by a cyclone and an anticyclone. SWP1 and SWP4 are
 380 with high T2 and RH induced by the southerly flow. While under SWP5, the YRD is with high T2
 381 and low RH because of the northerly flows are weakened and could not carry sufficient water vapor.
 382 SWP2 is with relatively low T2. SWP3 is under the control of a cyclone and the strong upward
 383 motion, it is with weak SR and low T2. Specific figures of atmospheric circulation at 850 hPa under
 384 the five SWPs are provided in the supplement.

385

386 **TABLE 1. The occurrence days and frequency, typical characteristics, regional mean \pm the**
 387 **standard error for T2, RH, WS and SR and positive and negative days under each SWP. The $>$**
 388 **0 and > 0.5 represent the value of EOF1 time series more than 0 and 0.5, respectively. The < 0**
 389 **and < 0.5 is on the contrary.**

Type and number of days (frequency)	Typical characteristic of SWPs	Meteorological factors	Pos (>0 and >0.5) Neg (<0 and <0.5) (number of days)
SWP1 372 (41.43%)	Southwesterly flow introduced by WPSH	T2($^{\circ}$ C): 28.38 \pm 4.94	175, 112 194, 125
		RH (%): 77.98 \pm 10.44	
		WS (m/s): 7.30 \pm 0.54	
		SR (W/m 2): 1606.20 \pm 537.77	
SWP2 209 (23.27%)	Northwesterly flow introduced by a continental high pressure and the Aleutian low pressure	T2 ($^{\circ}$ C): 26.40 \pm 5.37	110, 73 97, 57
		RH (%): 73.97 \pm 12.85	
		WS (m/s): 7.28 \pm 0.51	
SWP3 70 (7.80%)	an extratropical cyclone	T2 ($^{\circ}$ C): 25.41 \pm 4.37	12, 6 58, 45
		RH (%): 86.80 \pm 6.25	

		WS (m/s): 7.33 ± 0.58	
		SR (W/m ²): 959.73 ± 478.14	
SWP4	Southeasterly flow brought by WPSH and a southern cyclone system	T2 (°C): 29.29 ± 4.24 RH (%): 78.67 ± 8.51 WS (m/s): 7.11 ± 0.56 SR (W/m ²): 1505.97 ± 538.96	46, 30 82, 58
128 (14.25%)			
SWP5	The north China anticyclone system	T2(°C): 28.08 ± 4.99 RH (%): 73.97 ± 12.03 WS (m/s): 7.22 ± 0.45 SR (W/m ²): 1586.78 ± 479.65	40, 24 23, 14
64 (7.13%)			
others	/	/	/
55 (6.12%)			

390

391 3.3.2. Impacts of SWP change on O₃ concentration variation

392 We explore the impacts of SWP change on O₃ variation through an analysis combined with
393 EOF. As illustrated in section 3.1.2, the EOF1 mode is the dominant mode, and it implies the
394 increase of O₃ in the entire YRD is the main trend. The EOF1 time series is closely correlated to the
395 regional mean O₃ concentration ($R = 0.98$). In this study, we primarily focus on why O₃
396 concentration increases in the entire YRD region, rather than on why the increases in O₃ differ
397 spatially inside the YRD. Therefore, we use the EOF1 time series as a proxy to present the regional
398 O₃ concentration. In Table 1, the positive phase (Pos) represents that the EOF1 time series is more
399 than 0 and it is beneficial to the production and accumulation of O₃. On the contrary, the negative
400 phase (Neg) corresponds low O₃ concentrations. We extract the information by comparing Pos with
401 Neg to find the changes in each SWP. Yin et al. (2019) explored dominant patterns of summer O₃
402 pollution and associated atmospheric circulation changes in eastern China. Differently from their
403 study, we analyzed the daily variation in SWPs, and thus identified the change in atmospheric
404 circulations more precisely.

405 In the five main SWPs, the EOF1 time series show an increase trend during their occurrence
406 days in the warm seasons. It means that the five main SWPs tend to bring high ambient O₃

407 concentration through changes in the SWPs, which include SWP changes in both frequency and
 408 intensity. We find that the change in SWP intensity impacts more significantly the inter-annual
 409 variation in O₃ levels than the change in SWP frequency, consistent with the results of Hegarty et
 410 al. (2007) and Liu et al. (2019). This will be further discussed in section 3.4. In the following, we
 411 will concretely discuss the variation characteristics of the five SWPs and their impacts on the
 412 increase of O₃ in the YRD. Especially, we will show atmospheric circulations at 850 hPa and 500
 413 hPa, meteorological factors including SR, T2, LCC, TCLW, RH, meridional wind at 850hPa (V850)
 414 and W (vertical velocity) under positive and negative phase of all SWPs, and correlation coefficients
 415 of RH, SR and T2 with EOF1 time series under all SWPs.

416 As shown in previous study, SR, T2 and RH are dominated meteorological factors and can
 417 directly impact O₃ photochemical formation and loss (Xie et al. 2017; Gao et al. 2020). To explore
 418 the importance and difference of their impacts on O₃ concentrations under different SWPs, we
 419 calculate the correlation coefficients between the EOF1 time series and these meteorological factors
 420 under each SWP. As shown in table 2 and 3, when the absolute values of the calculated correlation
 421 coefficients under a SWP are greater than 0.4, the corresponding meteorological factors present
 422 significant changes between Pos and Neg phases. Therefore, we regard them as the crucial
 423 meteorological factors that impact O₃ variation under that SWP. In the end, we find that significant
 424 decreases in RH and increases in SR are the crucial meteorological factors under SWP1, SWP4 and
 425 SWP5. For SWP2, significant decreases in RH, increases in SR and T2 are the crucial
 426 meteorological factors. For SWP3, significant decreases in RH is the crucial meteorological factor.
 427 Hereinafter, we discuss variations in crucial meteorological factors induced by change in
 428 atmospheric circulations.

429

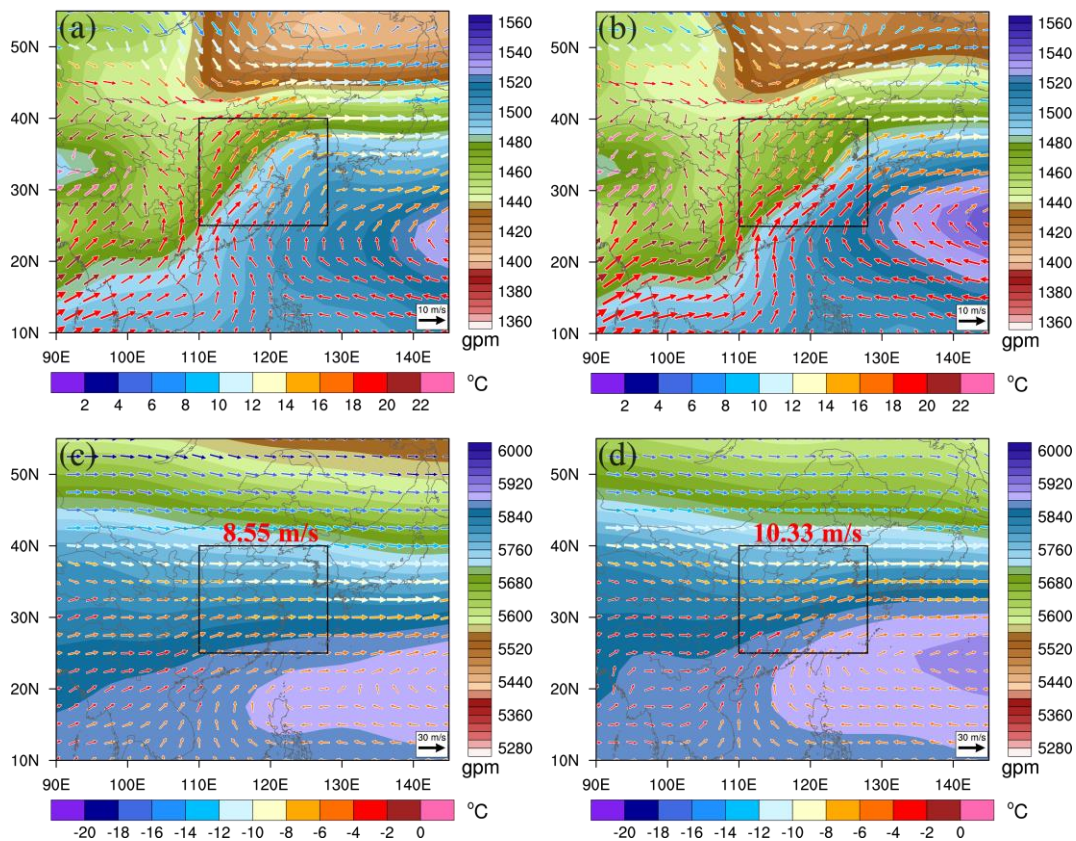
430 **TABLE 2. Correlation coefficients of RH, SR and T2 with EOF1 time series under each SWP.**

Variable	SWP1	SWP2	SWP3	SWP4	SWP5
RH	-0.59	-0.52	-0.50	-0.64	-0.59
SR	0.58	0.56	0.33	0.46	0.48
T2	0.19	0.41	0.26	0.15	0.30

431

432 Fig. 4 shows the atmospheric circulations at 850 hPa and 500 hPa, and Table 3 shows
 433 meteorological factors including SR, T2, TCC, TCLW, RH, V850 and W for SWP1_Pos and

434 SWP1_Neg. As shown in Figs. 4a and 4b, the YRD is located at the northwest of the WPSH, mainly
 435 affected by the southwesterly winds. Due to the weakening of the WPSH, compared with V850 of
 436 4.27 m/s under SWP1_neg, weakening V850 of 2.89 m/s under SWP1_pos bring a less amount of
 437 water vapor to YRD region, therefore, RH significantly decreases by 15.24%. At 500 hPa, a shallow
 438 trough located at approximate 113°E is replaced by a slowly straight westerly flow, and the
 439 downward motion would strengthen and last longer. Besides, significant decreases in RH under the
 440 downward motion condition hinder cloud formation. LCC and TCLW decrease by 0.30 and 0.04,
 441 respectively. Furthermore, SR significantly increases by 730.04 W/m² due to the less shelter of the
 442 clouds and less reflection above the cloud. Eventually, significant decreases in RH and increases in
 443 SR lead to stronger O₃ photochemical reaction.
 444



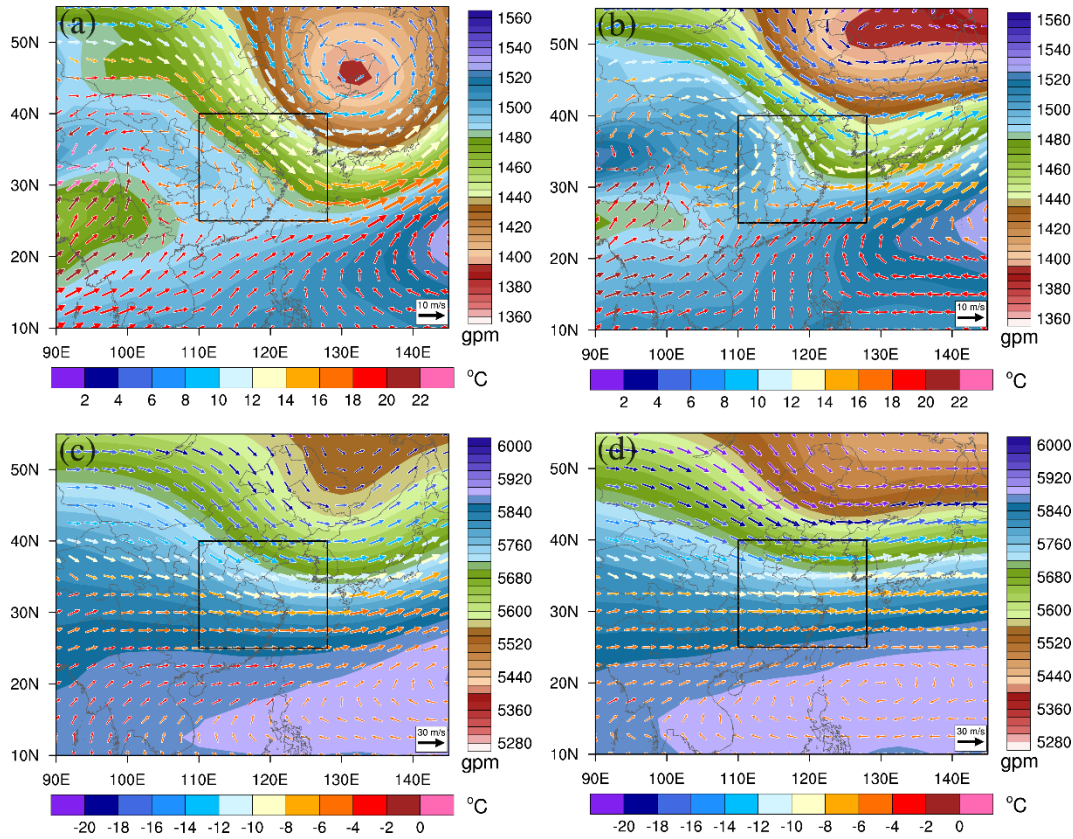
445
 446 **Fig. 4. The geopotential height (shaded) and 850 hPa wind with temperature (color vector)**
 447 **under (a) SWP1_Pos and (b) SWP1_Neg. The geopotential height (shaded) and 500 hPa wind**
 448 **with temperature (color vector) under (c) SWP1_Pos and (d) SWP1_Neg. The red values**
 449 **represent the regionally averaged wind speed at 500 hPa in the zone around black lines. The**

450 **boxed area in Figs. 4a-d encloses the YRD.**

451

452 Fig. 5 shows the atmospheric circulations at 850 hPa and 500 hPa, and Table 3 shows
453 meteorological factors including SR, T2, TCC, TCLW, RH, V850 and W for SWP2_Pos and
454 SWP2_Neg. As shown in Figs. 5a and 5b, the YRD is affected by a continental high and the Aleutian
455 low, characterized by northwesterly flow and a bit southwesterly flow. Compared with the
456 SWP2_Neg, the continental high in SWP2_Pos is weakening. Therefore, the YRD region is
457 influenced by warm flows and T2 significantly increases by 4.91 °C. The correlation between the
458 EOF1 time series and T2 under SWP2 ($R_{T2-SWP2} = -0.41$) is closer than the correlation in the whole
459 period ($R_{T2-all} = -0.24$). This implies that the weakening of the continental high plays an important
460 role in enhancing O₃ there. Meanwhile, as the Aleutian low moves southward slightly, the
461 southwesterly flow can hardly bring water vapor to the YRD, which leads to significant decreases
462 in RH by 14.79%. At 500 hPa, a trough located at approximate 120°E–125°E is strengthened
463 associated with Aleutian low shifting southward, leading to the stronger downward motion in the
464 northwestern YRD behind the strengthening trough. Just like SWP1, stronger downward motion
465 and significantly decreasing RH enhance SR significantly by 790.06 W/m². Significant decreases
466 in RH, increases in SR and T2 are beneficial to O₃ formation.

467



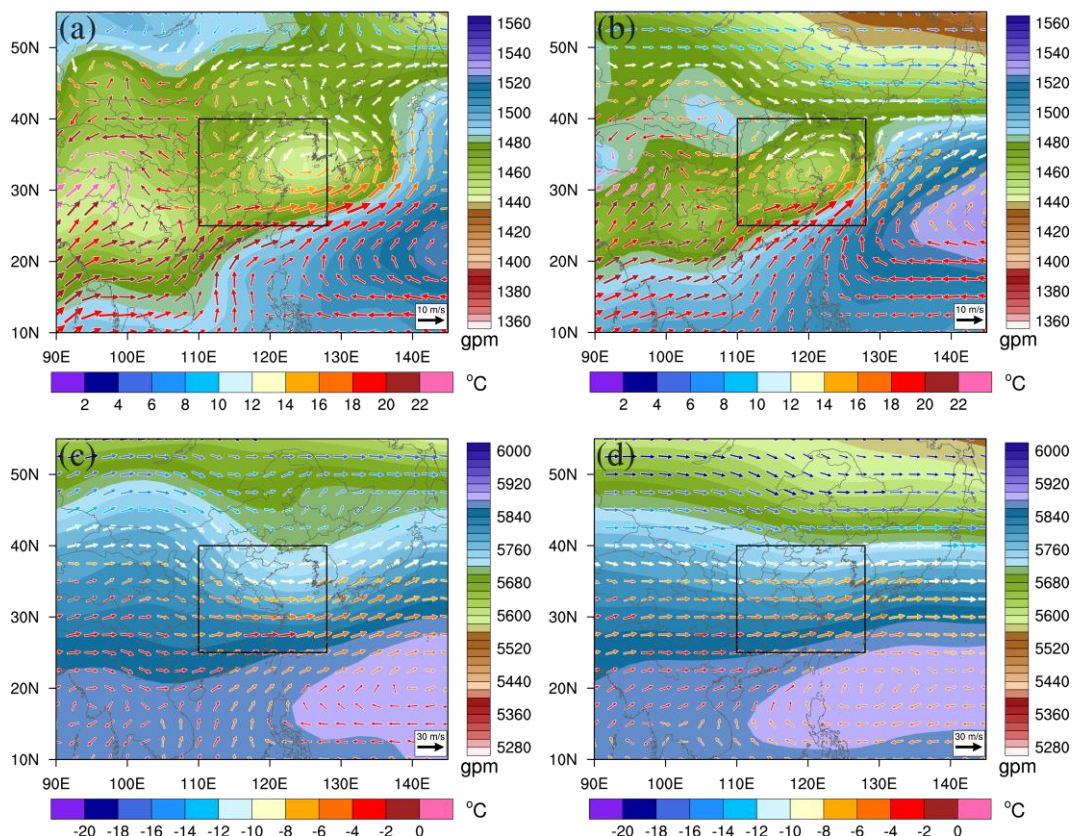
468

469 **Fig. 5. The geopotential height (shaded) and 850 hPa wind with temperature (color vector)**
 470 **under (a) SWP2_Pos and (b) SWP2_Neg. The geopotential height (shaded) and 500 hPa wind**
 471 **with temperature (color vector) under (c) SWP2_Pos and (d) SWP2_Neg. The boxed area in**
 472 **Figs. 5a-d encloses the YRD.**

473

474 Fig. 6 shows the atmospheric circulations at 850 hPa and 500 hPa, and Table 3 shows
 475 meteorological factors including SR, T2, TCC, TCLW, RH, V850 and W for SWP3_Pos and
 476 SWP3_Neg. As shown in Figs. 6a and 6b, the YRD is controlled by an extratropical cyclone.
 477 Compared with the SWP3_Neg, the low pressure in SWP3_Pos strengthens and its location is
 478 slightly further eastward. Under this circumstance, the weakening southerly flow could hardly bring
 479 water vapor to the YRD and thus RH significantly decreases by 11.73%. At 500 hPa, the upward
 480 motion would be weakening due to the eastern movement of cyclone and western area controlled
 481 by back of a strengthening trough located at about 120°E. However, LCC still is at a high level
 482 under upward motion condition. Furthermore, high LCC and its less variation lead to low SR.
 483 Therefore, the correlation coefficient between SR and EOF1 time series is relatively low under this

484 SWP3 ($R_{SR-SWP3}=-0.33$). Lastly, only significant decreases in RH would be crucial factor for high
 485 O_3 concentration.
 486

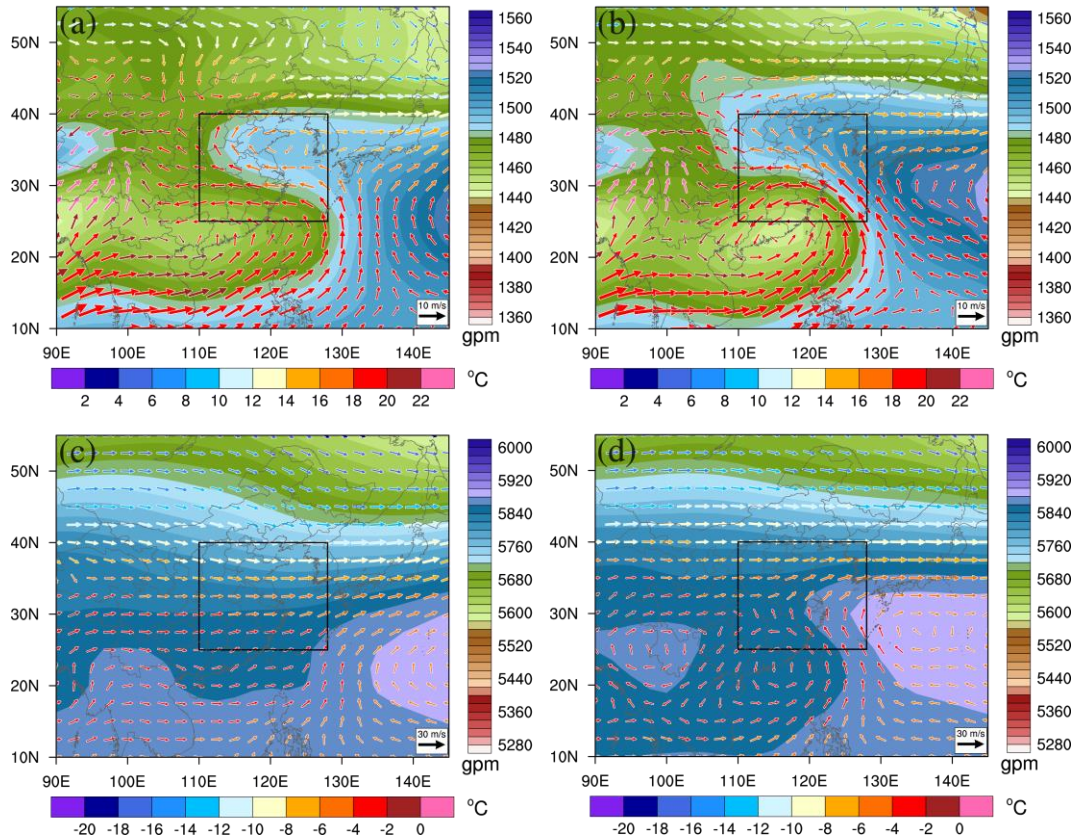


487
 488 **Fig. 6. The geopotential height (shaded) and 850 hPa wind with temperature (color vector)**
 489 **under (a) SWP3_Pos and (b) SWP3_Neg. The geopotential height (shaded) and 500 hPa wind**
 490 **with temperature (color vector) under (c) SWP3_Pos and (d) SWP3_Neg. The boxed area in**
 491 **Figs. 6a-d encloses the YRD.**

492
 493 Fig. 7 shows the atmospheric circulations at 850 hPa and 500 hPa, and Table 3 shows
 494 meteorological factors including SR, T2, LCC, TCLW, RH, V850 and W for SWP4_Pos and
 495 SWP4_Neg. As shown in Figs. 7a and 7b, southeasterly winds prevail in the YRD, which is
 496 modulated by a southern low pressure and WPSH. Compared with the SWP4_Neg, the southern
 497 low pressure and southeasterly flow in SWP4_Pos is weaker, and thus it brings less water vapor to
 498 the YRD and significantly decreases RH by 12.26%. At 500 hPa, a shallow trough located at about
 499 125°E strengthens associated with weakening of the southern cyclone pressure, causing the strong
 500 sink motion, less LCC and significant increases in SR by 538.53 W/m². Significant increases in SR

501 and decreases in RH are important for O₃ pollution.

502



503

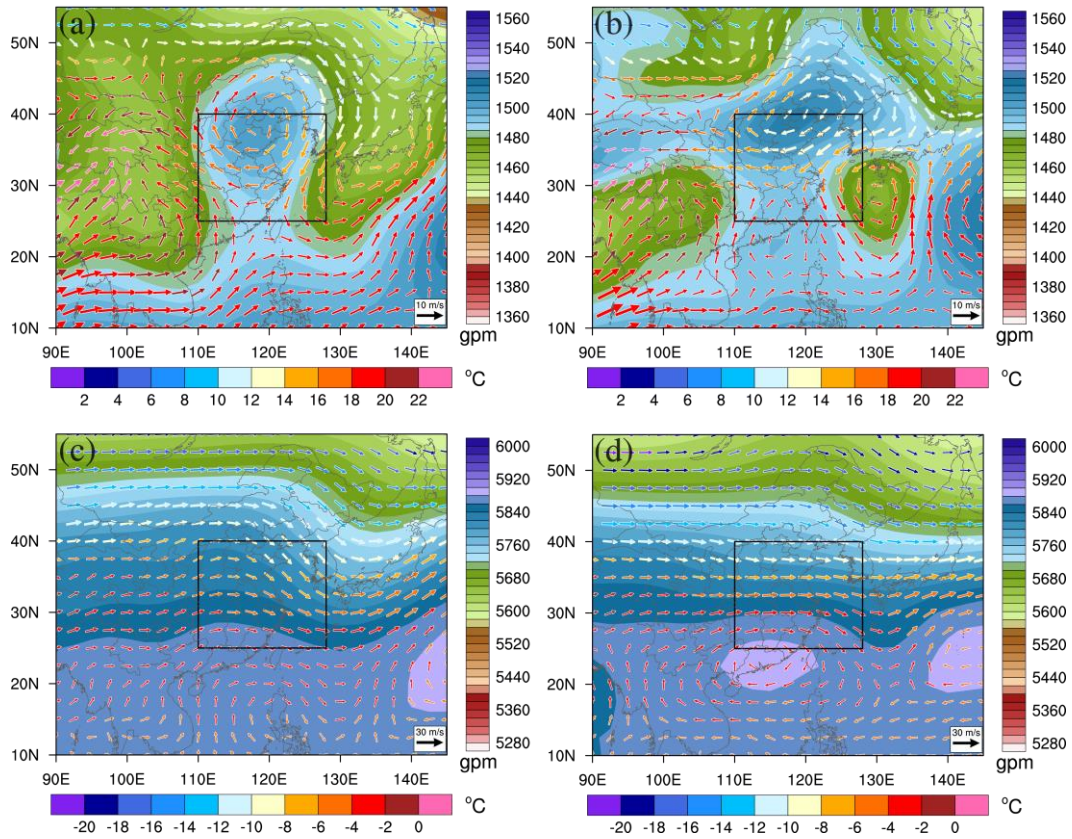
504 **Fig. 7. The geopotential height (shaded) and 850 hPa wind with temperature (color vector)**
505 **under (a) SWP4_Pos and (b) SWP4_Neg. The geopotential height (shaded) and 500 hPa wind**
506 **with temperature (color vector) under (c) SWP4_Pos and (d) SWP4_Neg. The boxed area in**
507 **Figs. 7a-d encloses the YRD.**

508

509 Fig. 8 shows the atmospheric circulations at 850 hPa and 500 hPa, and Table 3 shows
510 meteorological factors including SR, T2, LCC, TCLW, RH, V850 and W for SWP5_Pos and
511 SWP5_Neg. As shown in Figs. 8a and 8b, the YRD is controlled by the north China anticyclone,
512 characterized by the northeasterly and the southwesterly winds. Compared with the SWP5_Neg, the
513 high pressure in the SWP5_Pos is weaker and the northeasterly flow respond accordingly. The
514 weakened sea flow makes air dryer and RH significantly lower by 17.34%. At 500hPa, a trough
515 located at about 130°E controlling the YRD strengthens associated the Japan low pressure
516 appearance. The downward motions become strong correspondingly and result in significant
517 increases in SR by 628.26 W/m². Significant increases in SR and decreases in RH lead to increases

518 in O₃ concentration.

519



520

521 **Fig. 8.** The geopotential height (shaded) and 850 hPa wind with temperature (color vector)
 522 under (a) SWP5_Pos and (b) SWP5_Neg. The geopotential height (shaded) and 500 hPa wind
 523 with temperature (color vector) under (c) SWP5_Pos and (d) SWP5_Neg. The boxed area in
 524 **Figs.8a-d** encloses the YRD.

525

526 **TABLE 3.** Regional mean \pm the standard error of meteorological factors in Pos and Neg
 527 phases and their difference under each SWP pattern.

SWP	phase	RH (%)	SR (W/m ²)	T2 (°C)	LCC	TCLW	V850 (m/s)	W (Pa/s)
P1	Pos	69.70±9.69	1970.97±403.19	29.90±4.76	0.07±0.15	0.06±0.08	2.89±2.24	0.00±0.05
	Neg	84.94±6.53	1240.93±460.18	27.45±4.78	0.37±0.27	0.17±0.14	4.27±2.73	-0.05±0.05
	Diff	-15.24	730.04	2.45	-0.30	-0.11	-1.38	0.05
P2	Pos	66.49±10.96	1968.41±377.12	28.81±4.32	0.07±0.14	0.06±0.09	-2.47±3.09	0.02±0.05
	Neg	81.29±10.78	1178.34±479.58	23.89±5.90	0.48±0.31	0.19±0.14	-1.37±3.21	-0.03±0.06
	Diff	-14.79	790.06	4.91	-0.41	-0.13	-1.10	0.05
P3	Pos	76.89±7.09	1371.42±605.82	27.83±2.45	0.34±0.18	0.21±0.19	-0.67±3.43	-0.02±0.04
	Neg	88.62±5.14	854.96±395.09	24.77±4.58	0.58±0.24	0.31±0.16	1.93±3.65	-0.09±0.06

	Diff	-11.73	516.45	3.06	-0.24	-0.10	-2.60	0.07
	Pos	71.11±7.15	1882.33±388.10	30.62±3.69	0.11±0.16	0.12±0.16	0.57±2.40	0.01±0.04
P4	Neg	83.37±6.76	1343.80±547.50	28.93±4.19	0.35±0.24	0.19±0.19	2.46±3.60	-0.04±0.06
	Diff	-12.26	538.53	1.69	-0.24	-0.07	-1.89	0.05
	Pos	68.47±14.19	1827.46±447.37	29.60±5.25	0.07±0.11	0.09±0.14	-1.83±3.42	0.01±0.04
P5	Neg	85.81±3.45	1199.21±397.17	26.43±3.82	0.43±0.30	0.16±0.09	-2.31±5.25	-0.02±0.04
	Diff	-17.34	628.26	3.17	-0.35	-0.07	0.48	0.03
Others		/	/	/	/	/	/	/

528

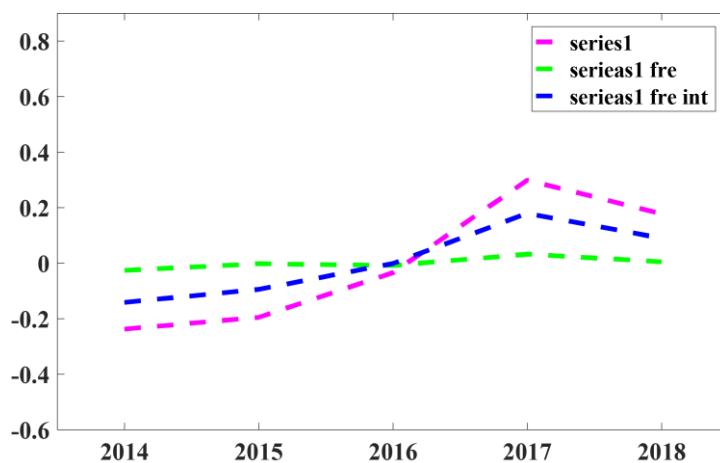
529 **3.4. Indicators for reconstructing inter-annual O₃ variation affected by synoptic-scale** 530 **atmospheric circulation**

531 Due to the similar variations in regional mean O₃ concentration and EOF1 time series, we
532 have reconstructed the inter-annual EOF1 time series to replace the regional mean O₃ concentration
533 by accounting either frequency-variation-only or both frequency and intensity variations in SWPs,
534 which are EOF1 time series (Fre) and EOF1 time series (Fre + Int), respectively. The observed and
535 reconstructed inter-annual EOF1 time series in 2014–2018 over the entire YRD region are shown
536 in Fig. 9. Obviously, the frequency changes in SWPs almost have no impact on the O₃ variability in
537 the entire YRD. However, considering intensity change, the fitting curve would be closer to the
538 EOF1 time series. To obtain the accurate frequency and intensity change contributions, quantitative
539 evaluation is carried out, we define the contribution index as the difference between the maximum
540 and the minimum of a certain reconstructed time series divided by the difference between the
541 maximum and the minimum of inter-annual EOF1 time series: Contribution Index = (The
542 reconstructed maximum – the reconstructed minimum)/(the original maximum – the original
543 minimum). Through the above equation, we derive the relative contribution (contribution index) of
544 the frequency change and the intensity change. Compared with the contribution index of 10.86%
545 for SWPs frequency change, the value of 48.89% for SWPs intensity change accounts for a larger
546 proportion. Therefore, the intensity change in SWP is more important to the inter-annual O₃
547 variation than the frequency change.

548 During the reconstructed process, we drastically found that SWPIIs (SWP intensity indexes)
549 definition play an important role to reconstructing curve. In previous studies, Hegarty et al. (2007)
550 and Liu et al. (2019) reconstructed the inter-annual O₃ level in the northeastern United States and
551 the northern China using the same method as ours. They defined the intensity change in SWPs using

552 the domain-averaged sea level pressure and the pressure of the lowest-pressure system. However,
553 the correlation under Hegarty's Pattern V is poor, which has negative effect on their reconstructed
554 curve. Therefore, we select six SWPIIs and judge their rationality through their correlation
555 coefficients with EOF1 time series under each SWP: the maximum geopotential height in zone 1
556 (25°N–40°N, 110°E–130°E) and zone 2 (20°N–50°N, 90°E–140°E), the minimum geopotential
557 height in zone 1 (25°N–40°N, 110°E–130°E) and zone 2 (20°N–50°N, 90°E–140°E), and the
558 average geopotential height in zone 1 (25°N–40°N, 110°E–130°E) and zone 3 (10°N–40°N, 110°E–
559 130°E). As shown in Table 2, for SWP3 and SWP5, the SWPII for the maximum geopotential height
560 in zone 1 has a relative high correlation. For SWP1 and SWP4, the SWPII for the maximum
561 geopotential height in zone 2 has a relative high correlation. we found that the maximum
562 geopotential height show a relatively close correlation with the annual EOF1 time series. It is
563 because the maximum geopotential height reflects the wind speed affecting water vapor transport
564 under this pattern. Compared with SWP3 and SWP5, the weather systems are larger than the
565 classification region for SWP1 and SWP4. So it shows better correlation coefficients in the large
566 zone 2 than in zone 1 under SWP1 and SWP4. For SWP2, when O₃ concentration tends to be at a
567 high level, a cold continental high behind the YRD tends to weaken. Therefore, we select the average
568 geopotential height in zone 3 to represent the SWPII. Table 4 shows that the reconstructed curve
569 becomes good when we select different SWPIIs according to the characteristics of high O₃ level
570 under each SWP.

571



572

573 **Fig. 9. The trend of the inter-annual EOF1 time series in the warm seasons. The pink curve**
574 **represents the original inter-annual EOF1 time series in the warm seasons, the green line**

575 represents the reconstructed EOF1 time series only accounting the frequency variation in
 576 SWPs, and blue line represents the reconstructed one accounting both the frequency and the
 577 intensity variations in SWPs.

578

579 **TABLE 4. Correlation coefficients between EOF1 time series and different SWPIIs under each**
 580 **SWP.**

Type	Z _{1-ave}	Z _{1-max}	Z _{1-min}	Z _{2-min}	Z _{2-max}	Z _{3-ave}
SWP1	-0.47	-0.29	-0.35	-0.33	-0.60	-0.32
SWP2	-0.14	-0.08	0.02	-0.07	-0.09	-0.40
SWP3	0.28	0.61	0.03	0.05	0.43	-0.60
SWP4	-0.14	-0.03	-0.17	-0.22	0.78	-0.38
SWP5	0.52	0.76	0.39	0.56	0.72	0.58

581

582 **4. Conclusions and discussions**

583 In this study, we discussed meteorological influences on the O₃ variation in the warm seasons
 584 during 2014–2018 in the YRD, China. Specifically, we analyzed the O₃ spatio-temporal distribution
 585 characteristics, quantified the contribution of meteorological conditions to the O₃ variations,
 586 explored how changes in SWPs and corresponding meteorological factors lead to O₃ increase in the
 587 YRD over 2014–2018, and assessed the contributions of SWP frequency and intensity to the inter-
 588 annual O₃ variation in the region. The main conclusions are as follows.

589 The annual mean O₃ concentrations during the warm seasons averaged over the YRD are 32.49,
 590 33.03, 35.14, 37.44 and 35.98 ppb, respectively, for each year from 2014 to 2018, with a
 591 significantly increasing rate of 1.81 ppb year⁻¹ (5.21% year⁻¹). Meanwhile, the total number of days
 592 on which O₃ concentration exceeding the national standard also increases with year in a similar
 593 pattern. Through the EOF analysis of O₃ in space and time, three dominant modes were identified.
 594 The first mode is the most dominant mode, accounting for 65.7% of the O₃ variation, suggesting
 595 that increase tendencies in O₃ prevail over the entire YRD.

596 We quantified the influence of meteorology on the inter-annual variation and trend of O₃ over
 597 the YRD from 2014–2018, and found that the influence could lead to a regional O₃ increase by 3.03

598 ppb at most. Especially, RH plays the most important role in modulating the inter-annual O₃
599 variation, followed by SR and LCC. RH impacts on O₃ concentration through two ways. One is gas
600 phase H₂O reacting with O₃ ($O_3 + H_2O(gas) + hv \rightarrow O_2 + 2OH$). The other is its influencing on
601 clouds and thereby shielding SR. To explore connections between the O₃ variation and synoptic
602 circulations, we further identified nine types of SWPs objectively based on the PTT method, and
603 selected five main types to explore their impact on O₃ variation. The typical weather systems of the
604 five SWPs include the WPSH under SWP1, a continental high and the Aleutian low under SWP2,
605 an extratropical cyclone under SWP3, a southern low pressure and the WPSH under SWP4 and the
606 north China anticyclone under SWP5. Combining EOF1 time series variation under each SWP, we
607 found that the variation in all SWPs over 2014–2018 are favorable to O₃ increase during that period.
608 However, the crucial changes in meteorological factors attributable to the increases in O₃
609 concentrations are different under each SWP. For SWPs 1, 4 and 5, the crucial changes in
610 meteorological factors include significant decreases in RH and increases in SR, which are
611 predominantly attributable to the WPSH weakening under SWP1, the southern low pressure
612 weakening under SWP4, and the north China anticyclone weakening under SWP5. These changes
613 in weather systems prevent the water vapor from being transported to the YRD and result in RH
614 significantly decreased by 15.24, 12.26 and 17.34%, respectively. Moreover, the significant
615 decreases in RH and increases in downward motion (behind the strengthening trough and in front
616 of the strengthening ridge) lead to less LCC, and thereby SR significantly increases by 730.04,
617 538.53 and 628.26 W/m², respectively. Under SWP2, the crucial changes in meteorological factors
618 are significant decrease in RH by 14.79%, and increases in SR by 790.06 W/m² and T2 by 4.91 °C.
619 Significant decrease in RH and increases in SR are mainly induced by the Aleutian low southward
620 extending, which has a similar influential mechanism between RH, LCC and SR with SWPs 1, 4
621 and 5. In addition, significantly increases in T2 would be due to weakening cold flow introduced by
622 a weakening continental high. Under SWP3, the significant decreases in RH by 11.73% is mainly
623 induced by an intensified extratropical cyclone that blocks the southerly flow carrying water vapor
624 into the YRD. All changes are critical to O₃ formation under each SWP.

625 As the overall change in SWP intensity and that in SWP frequency contribute to 48.89% and
626 10.86% to the changes in O₃, we conclude that the change in SWP intensity is more important to

627 the O₃ increase over 2014–2018 than that in SWP frequency. We further reconstructed the EOF1
628 time series by considering different SWPIIs due to the unique characteristics of each SWP. The
629 results are better than those in Hegarty et al. (2007) and Liu et al. (2019) who used the same SWPIIs
630 in all SWPs.

631 This study quantified the inter-annual variation and increasing rate of O₃ in the YRD, China,
632 and explored the connection between SWP variations and the O₃ increase. It provides an enhanced
633 understanding of response of O₃ variation to changes in SWPs from year to year and thus this
634 understanding may be insightful to planning strategies for O₃ pollution control.

635

636 **Authorship contribution statement**

637 **Da Gao:** Conceptualization, Data curation, Formal analysis, Meteorology, Investigation,
638 software, Writing – original draft, Writing – revision. **Min Xie:** Conceptualization, Methodology,
639 Writing – revision, Project administration, Funding acquisition. **Jane Liu:** Formal analysis,
640 Meteorology, Writing – revision. **Tijian Wang:** Formal analysis, Funding acquisition. **Chaoqun**
641 **Ma:** Formal analysis, Meteorology. **Haokun Bai:** Formal analysis, Meteorology. **Xing Chen:**
642 Formal analysis. **Mengmeng Li:** Formal analysis. **Bingliang Zhuang:** Formal analysis. **Shu Li:**
643 Formal analysis

644

645 **Declaration of competing interest**

646 The authors declare that they have no known competing financial interests or personal
647 relationships that could have appeared to influence the work reported in this paper.

648

649 **Acknowledgements**

650 This work was supported by the National Key Research and Development Program of China
651 (2018YFC0213502, 2018YFC1506404).

652

653 **References**

654 Barnes, E. A., and Fiore, A. M.: Surface ozone variability and the jet position: Implications for projecting
655 future air quality, *Geophys Res Lett*, 40, 2839–2844, 10.1002/grl.50411, 2013.
656 Cooper, O. R., Schultz, M. G., Schroder, S., Chang, K. L., Gaudel, A., Benitez, G. C., Cuevas, E., Frohlich, M.,
657 Galbally, I. E., Molloy, S., Kubistin, D., Lu, X., McClure-Begley, A., Nedelec, P., O'Brien, J., Oltmans, S. J.,

658 Petropavlovskikh, I., Ries, L., Senik, I., Sjoberg, K., Solberg, S., Spain, G. T., Spangl, W., Steinbacher, M.,
659 Tarasick, D., Thouret, V., and Xu, X. B.: Multi-decadal surface ozone trends at globally distributed remote
660 locations, *Elementa-Sci Anthropol*, 8, Artn 23 10.1525/Elementa.420, 2020.

661 Day, D. B., Xiang, J., and Mo, J.: Association of ozone exposure with cardiorespiratory pathophysiological
662 mechanisms in healthy adults (vol 177, pg 1344, 2017), *Jama Intern Med*, 177, 1400-1400,
663 10.1001/jamainternmed.2017.4605, 2017.

664 Doherty, R. M., Wild, O., Shindell, D. T., Zeng, G., MacKenzie, I. A., Collins, W. J., Fiore, A. M., Stevenson, D.
665 S., Dentener, F. J., Schultz, M. G., Hess, P., Derwent, R. G., and Keating, T. J.: Impacts of climate change on
666 surface ozone and intercontinental ozone pollution: A multi-model study, *J Geophys Res-Atmos*, 118,
667 3744-3763, 10.1002/jgrd.50266, 2013.

668 Eskridge, R. E., Ku, J. Y., Rao, S. T., Porter, P. S., and Zurbenko, I. G.: Separating different scales of motion in
669 time series of meteorological variables, *B Am Meteorol Soc*, 78, 1473-1483, Doi 10.1175/1520-
670 0477(1997)078<1473:Sdsomi>2.0.Co;2, 1997.

671 Fiore, A. M., Jacob, D. J., Mathur, R., and Martin, R. V.: Application of empirical orthogonal functions to
672 evaluate ozone simulations with regional and global models, *J Geophys Res-Atmos*, 108, Artn 4431
673 10.1029/2002jd003151, 2003.

674 Gao, D., Xie, M., Chen, X., Wang, T. J., Liu, J., Xu, Q., Mu, X. Y., Chen, F., Li, S., Zhuang, B. L., Li, M. M., Zhao,
675 M., and Ren, J. Y.: Systematic classification of circulation patterns and integrated analysis of their effects
676 on different ozone pollution levels in the Yangtze River Delta Region, China, *Atmos Environ*,
677 <https://doi.org/10.1016/j.atmosenv.2020.117760> 2020.

678 Gao, W., Tie, X. X., Xu, J. M., Huang, R. J., Mao, X. Q., Zhou, G. Q., and Chang, L. Y.: Long-term trend of O₃ in
679 a mega City (Shanghai), China: Characteristics, causes, and interactions with precursors, *Sci Total Environ*,
680 603, 425-433, 10.1016/j.scitotenv.2017.06.099, 2017.

681 Han, H., Liu, J. E., Shu, L., Wang, T. J., and Yuan, H. L.: Local and synoptic meteorological influences on daily
682 variability in summertime surface ozone in eastern China, *Atmos Chem Phys*, 20, 203-222, 10.5194/acp-
683 20-203-2020, 2020.

684 He, J. J., Gong, S. L., Yu, Y., Yu, L. J., Wu, L., Mao, H. J., Song, C. B., Zhao, S. P., Liu, H. L., Li, X. Y., and Li, R. P.:
685 Air pollution characteristics and their relation to meteorological conditions during 2014-2015 in major
686 Chinese cities, *Environ Pollut*, 223, 484-496, 10.1016/j.envpol.2017.01.050, 2017.

687 Hegarty, J., Mao, H., and Talbot, R.: Synoptic controls on summertime surface ozone in the northeastern
688 United States, *J Geophys Res-Atmos*, 112, Artn D14306 10.1029/2006jd008170, 2007.

689 Hou, X. W., Zhu, B., Kumar, K. R., and Lu, W.: Inter-annual variability in fine particulate matter pollution over
690 China during 2013-2018: Role of meteorology, *Atmos Environ*, 214, ARTN 116842
691 10.1016/j.atmosenv.2019.116842, 2019.

692 Jacob, D. J., and Winner, D. A.: Effect of climate change on air quality, *Atmos Environ*, 43, 51-63,
693 10.1016/j.atmosenv.2008.09.051, 2009.

694 Jacob, D. J., and Winner, D. A.: Effect of climate change on air quality, *Atmos Environ*, 43, 51-63, 2009.

695 Jerrett, M., Burnett, R. T., Pope, C. A., Ito, K., Thurston, G., Krewski, D., Shi, Y. L., Calle, E., and Thun, M.: Long-
696 Term Ozone Exposure and Mortality., *New Engl J Med*, 360, 1085-1095, Doi 10.1056/Nejmoa0803894,
697 2009.

698 Leibensperger, E. M., Mickley, L. J., and Jacob, D. J.: Sensitivity of US air quality to mid-latitude cyclone
699 frequency and implications of 1980-2006 climate change, *Atmos Chem Phys*, 8, 7075-7086, DOI
700 10.5194/acp-8-7075-2008, 2008.

701 Li, K., Jacob, D. J., Liao, H., Shen, L., Zhang, Q., and Bates, K. H.: Anthropogenic drivers of 2013-2017 trends

702 in summer surface ozone in China, *P Natl Acad Sci USA*, 116, 422-427, 2019.

703 Liu, J. D., Wang, L. L., Li, M. G., Liao, Z. H., Sun, Y., Song, T., Gao, W. K., Wang, Y. H., Li, Y., Ji, D. S., Hu, B.,
704 Kerminen, V. M., Wang, Y. S., and Kulmala, M.: Quantifying the impact of synoptic circulation patterns on
705 ozone variability in northern China from April to October 2013-2017, *Atmos Chem Phys*, 19, 14477-
706 14492, 10.5194/acp-19-14477-2019, 2019.

707 Lu, X., Hong, J. Y., Zhang, L., Cooper, O. R., Schultz, M. G., Xu, X. B., Wang, T., Gao, M., Zhao, Y. H., and Zhang,
708 Y. H.: Severe Surface Ozone Pollution in China: A Global Perspective, *Environ Sci Tech Let*, 5, 487-494,
709 10.1021/acs.estlett.8b00366, 2018.

710 Lu, X., Zhang, L., Chen, Y. F., Zhou, M., Zheng, B., Li, K., Liu, Y. M., Lin, J. T., Fu, T. M., and Zhang, Q.: Exploring
711 2016-2017 surface ozone pollution over China: source contributions and meteorological influences,
712 *Atmos Chem Phys*, 19, 8339-8361, 10.5194/acp-19-8339-2019, 2019.

713 Lu, X., Zhang, L., Wang, X. L., Gao, M., Li, K., Zhang, Y. Z., Yue, X., and Zhang, Y. H.: Rapid Increases in Warm-
714 Season Surface Ozone and Resulting Health Impact in China Since 2013, *Environ Sci Tech Let*, 7, 240-
715 247, 10.1021/acs.estlett.0c00171, 2020.

716 Milanchus, M. L., Rao, S. T., and Zurbenko, I. G.: Evaluating the effectiveness of ozone management efforts
717 in the presence of meteorological variability, *J Air Waste Manage*, 48, 201-215, Doi
718 10.1080/10473289.1998.10463673, 1998.

719 Papanastasiou, D. K., Melas, D., Bartzanas, T., and Kittas, C.: Estimation of Ozone Trend in Central Greece,
720 Based on Meteorologically Adjusted Time Series, *Environ Model Assess*, 17, 353-361, 10.1007/s10666-
721 011-9299-6, 2012.

722 Philipp, A., Beck, C., Huth, R., and Jacobeit, J.: Development and comparison of circulation type
723 classifications using the COST 733 dataset and software, *Int J Climatol*, 36, 2673-2691, 10.1002/joc.3920,
724 2016.

725 Pu, X., Wang, T. J., Huang, X., Melas, D., Zanis, P., Papanastasiou, D. K., and Poupkou, A.: Enhanced surface
726 ozone during the heat wave of 2013 in Yangtze River Delta region, China, *Sci Total Environ*, 603, 807-
727 816, 10.1016/j.scitotenv.2017.03.056, 2017.

728 Rao, S. T., and Zurbenko, I. G.: Detecting And Tracking Changes In Ozone Air-Quality, *J Air Waste Manage*,
729 44, 1089-1092, Doi 10.1080/10473289.1994.10467303, 1994.

730 Rao, S. T., and Zurbenko, I. G.: Detecting And Tracking Changes In Ozone Air-Quality, *J Air Waste Manage*,
731 44, 1089-1092, Doi 10.1080/10473289.1994.10467303, 1994.

732 Santurtun, A., Gonzalez-Hidalgo, J. C., Sanchez-Lorenzo, A., and Zarrabeitia, M. T.: Surface ozone
733 concentration trends and its relationship with weather types in Spain (2001-2010), *Atmos Environ*, 101,
734 10-22, 10.1016/j.atmosenv.2014.11.005, 2015.

735 Shu, L., Xie, M., Wang, T. J., Gao, D., Chen, P. L., Han, Y., Li, S., Zhuang, B. L., and Li, M. M.: Integrated studies
736 of a regional ozone pollution synthetically affected by subtropical high and typhoon system in the
737 Yangtze River Delta region, China, *Atmos Chem Phys*, 16, 15801-15819, 10.5194/acp-16-15801-2016,
738 2016.

739 Shu, L., Xie, M., Gao, D., Wang, T. J., Fang, D. X., Liu, Q., Huang, A. N., and Peng, L. W.: Regional severe particle
740 pollution and its association with synoptic weather patterns in the Yangtze River Delta region, China,
741 *Atmos Chem Phys*, 17, 12871-12891, 10.5194/acp-17-12871-2017, 2017.

742 Shu, L., Wang, T., Han, H., Xie, M., Chen, P., Li, M., and Wu, H.: Summertime ozone pollution in the Yangtze
743 River Delta of eastern China during 2013-
744 2017: Synoptic impacts and source apportionment, *Environ. Pollut.*, 257, 113631, [https://doi.org/10.10](https://doi.org/10.1016/j.envpol.2019.113631)
745 [16/j.envpol.2019.113631](https://doi.org/10.1016/j.envpol.2019.113631), 2020.

746 Wang, B., and Fan, Z.: Choice of south Asian summer monsoon indices, *B Am Meteorol Soc*, 80, 629-638,
747 Doi 10.1175/1520-0477(1999)080<0629:Cosasm>2.0.Co;2, 1999.

748 Wang, B., Wu, Z. W., Li, J. P., Liu, J., Chang, C. P., Ding, Y. H., and Wu, G. X.: How to measure the strength of
749 the East Asian summer monsoon, *J Climate*, 21, 4449-4463, 10.1175/2008JCLI2183.1, 2008.

750 Wang, T., Xue, L. K., Brimblecombe, P., Lam, Y. F., Li, L., and Zhang, L.: Ozone pollution in China: A review of
751 concentrations, meteorological influences, chemical precursors, and effects, *Sci Total Environ*, 575, 1582-
752 1596, 10.1016/j.scitotenv.2016.10.081, 2017.

753 Wise, E. K., and Comrie, A. C.: Extending the Kolmogorov-Zurbenko filter: Application to ozone, particulate
754 matter, and meteorological trends, *J Air Waste Manage*, 55, 1208-1216, Doi
755 10.1080/10473289.2005.10464718, 2005.

756 Xie, M., Zhu, K. G., Wang, T. J., Yang, H. M., Zhuang, B. L., Li, S., Li, M. G., Zhu, X. S., and Ouyang, Y.: Application
757 of photochemical indicators to evaluate ozone nonlinear chemistry and pollution control
758 countermeasure in China, *Atmos Environ*, 99, 466-473, 10.1016/j.atmosenv.2014.10.013, 2014.

759 Xie, M., Liao, J., Wang, T., Zhu, K., Zhuang, B., Han, Y., Li, M., and Li, S.: Modeling of the anthropogenic heat
760 flux and its effect on regional meteorology and air quality over the Yangtze River Delta region, China,
761 *Atmospheric Chemistry and Physics*, 16, 6071-6089, 10.5194/acp-16-6071-2016, 2016a.

762 Xie, M., Zhu, K., Wang, T., Chen, P., Han, Y., Li, S., Zhuang, B., and Shu, L.: Temporal characterization and
763 regional contribution to O₃ and NO_x at an urban and a suburban site in Nanjing, China, *The Science of
764 the total environment*, 551-552, 533-545, 10.1016/j.scitotenv.2016.02.047, 2016b.

765 Xie, M., Shu, L., Wang, T.-j., Liu, Q., Gao, D., Li, S., Zhuang, B.-l., Han, Y., Li, M.-m., and Chen, P.-l.: Natural
766 emissions under future climate condition and their effects on surface ozone in the Yangtze River Delta
767 region, China, *Atmospheric Environment*, 150, 162-180, 10.1016/j.atmosenv.2016.11.053, 2017.

768 Yang, Y., Liao, H., and Li, J.: Impacts of the East Asian summer monsoon on interannual variations of
769 summertime surface-layer ozone concentrations over China, *Atmos Chem Phys*, 14, 6867-6879, 2014.

770 Yang, L. F., Luo, H. H., Yuan, Z. B., Zheng, J. Y., Huang, Z. J., Li, C., Lin, X. H., Louie, P. K. K., Chen, D. H., and
771 Bian, Y. H.: Quantitative impacts of meteorology and precursor emission changes on the long-term trend
772 of ambient ozone over the Pearl River Delta, China, and implications for ozone control strategy, *Atmos
773 Chem Phys*, 19, 12901-12916, 10.5194/acp-19-12901-2019, 2019.

774 Yarnal, B.: Synoptic Climatology in Environmental Analysis A Primer, *Journal of Preventive Medicine
775 Information*, 347, 170-180, 1993.

776 Yin, Z. C., Cao, B. F., and Wang, H. J.: Dominant patterns of summer ozone pollution in eastern China and
777 associated atmospheric circulations, *Atmos Chem Phys*, 19, 13933-13943, 10.5194/acp-19-13933-2019,
778 2019.

779 Yue, X., Unger, N., Harper, K., Xia, X. G., Liao, H., Zhu, T., Xiao, J. F., Feng, Z. Z., and Li, J.: Ozone and haze
780 pollution weakens net primary productivity in China, *Atmos Chem Phys*, 17, 6073-6089, 10.5194/acp-
781 17-6073-2017, 2017.

782 Zhang, J. X., Gao, Y., Luo, K., Leung, L. R., Zhang, Y., Wang, K., and Fan, J. R.: Impacts of compound extreme
783 weather events on ozone in the present and future, *Atmos Chem Phys*, 18, 9861-9877, 10.5194/acp-18-
784 9861-2018, 2018.

785 Zhao, Z. J., and Wang, Y. X.: Influence of the West Pacific subtropical high on surface ozone daily variability
786 in summertime over eastern China, *Atmos Environ*, 170, 197-204, 2017.

787